Xin, W., Xiong, C., Rodríguez-Zuluaga, J., Kervalishvili, G., Stolle, C., Wang, H. (2018): Climatology of the Occurrence Rate and Amplitudes of Local Time Distinguished Equatorial Plasma Depletions Observed by Swarm Satellite. - *Journal of Geophysical Research*, *123*, 4, pp. 3014—3026.

DOI: http://doi.org/10.1002/2017JA025072

Journal of Geophysical Research: Space Physics

RESEARCH ARTICLE
10.1002/2017JA025072

Key Points:
- Amplitude of EPDs is rarely related to the occurrence rate but to the background electron density and GPS signal loss
- Postmidnight EPDs are consistent phenomenon throughout the full solar cycle
- Evidences supporting the postmidnight EPDs are the combined results from the continuing of former EPDs and newborn ones

Correspondence to:
X. Wan and H. Wang,
iml_wobscene@whu.edu.cn;
h.wang@whu.edu.cn

Citation:
Wan, X., Xiong, C., Rodriguez-Zuluaga, J., Kervalishvili, G. N., Stolle, C., & Wang, H. (2018). Climatology of the occurrence rate and amplitudes of local time distinguished equatorial plasma depletions observed by Swarm satellite. *Journal of Geophysical Research: Space Physics*, *123*, 3014–3026. https://doi.org/10.1002/2017JA025072

Received 1 DEC 2017
Accepted 17 MAR 2018
Accepted article online 23 MAR 2018
Published online 13 APR 2018

Climatology of the Occurrence Rate and Amplitudes of Local Time Distinguished Equatorial Plasma Depletions Observed by Swarm Satellite

Xin Wan[1,2], Chao Xiong[2], Juan Rodriguez-Zuluaga[2,3], Guram N. Kervalishvili[2], Claudia Stolle[2,3], and Hui Wang[1]

[1]College of Electronic Information, Wuhan University, Wuhan, China, [2]GFZ German Research Centre for Geosciences, Potsdam, Germany, [3]Faculty of Science, University of Potsdam, Potsdam, Germany

Abstract In this study, we developed an autodetection technique for the equatorial plasma depletions (EPDs) and their occurrence and depletion amplitudes based on in situ electron density measurements gathered by Swarm A satellite. For the first time, comparisons are made among the detected EPDs and their amplitudes with the loss of Global Positioning System (GPS) signal of receivers onboard Swarm A, and the Swarm Level-2 product, Ionospheric Bubble Index (IBI). It has been found that the highest rate of EPD occurrence takes place generally between 2200 and 0000 magnetic local time (MLT), in agreement with the IBI. However, the largest amplitudes of EPD are detected earlier at about 1900–2100 MLT. This coincides with the moment of higher background electron density and the largest occurrence of GPS signal loss. From a longitudinal perspective, the higher depletion amplitude is always witnessed in spatial bins with higher background electron density. At most longitudes, the occurrence rate of postmidnight EPDs is reduced compared to premidnight ones; while more postmidnight EPDs are observed at African longitudes. CHAMP observations confirm this point regardless of high or low solar activity condition. Further by comparing with previous studies and the plasma vertical drift velocity from ROCSAT-1, we suggest that while the *F* region vertical plasma drift plays a key role in dominating the occurrence of EPDs during premidnight hours, the postmidnight EPDs are the combined results from the continuing of former EPDs and newborn EPDs, especially during June solstice. And these newborn EPDs during postmidnight hours seem to be less related to the plasma vertical drift.

Plain Language Summary Practically, the equatorial plasma depletions are always related to transionospheric radio signal interruption. However, this work reveals that the higher occurrence of the structure does not always coincident with the higher occurrence of Global Positioning System signal loss, but the larger depletion amplitude is required. From the scientific perspective, the mechanism behind postmidnight equatorial plasma depletions is varying, and this work provides proofs on some aspects about postmidnight equatorial plasma depletions.

1. Introduction

Equatorial plasma depletion (EPD) is a well-known phenomenon at equatorial and low latitudes during post-sunset hours, which are also referred to as equatorial plasma bubbles or equatorial spread *F* in other literature. The first awareness of this structure came from the observed *F* region diffuse echoes of vertical radio sounding over a wide range of wave-frequency near Huancayo, Peru (Booker & Wells, 1938). Since then extensive works have been put efforts on the subject. The generation of EPDs is a result of the Rayleigh-Taylor (R-T) instability (Hudson & Kennel, 1975; Ott, 1978; Sultan, 1996). Due to the absence of sunlight after sunset, the ionization density at *E* region decays rapidly, and the larger ion-neutral recombination rate at lower altitude further helps to create a steep vertical plasma density gradient toward the topside *F* region, which is opposite to the direction of the gravitational force. This kind of configuration is unstable, and if there are instabilities at the bottom side of *F* region (e.g., Kelley et al., 1981, 1986; Singh et al., 1997), these instabilities will be enhanced and drift upward and form plasma irregularities elongated along the magnetic flux tubes at the topside ionosphere.

Stolle et al. (2008) presented global evidence for the linear relationship between the EPD occurrence rate and the vertical plasma drift. Near sunset sector, the upward vertical $\mathbf{E} \times \mathbf{B}$ drift is greatly enhanced, commonly referred as the prereversal enhancement (PRE). The strength of the PRE is known to be correlated with the occurrence of premidnight (postsunset) EPDs (e.g., Carter et al., 2013; Dabas et al., 2003; Fejer et al., 1999;

Su et al., 2008). By comparing the vertical plasma drift with the EPDs of different scale sizes, Xiong et al. (2012) also found a good correlation between the integrated vertical plasma drift (during PRE) and the occurrence of EPDs. Additionally, the authors identified more structured EPDs in regions with higher upward drift velocity. As the strength of PRE significantly increases from solar minimum to solar maximum particularly during the equinoxes (Fejer et al., 1995), more EPDs are expected to occur during solar maximum periods (e.g., Basu et al., 1988, 2002). Huang et al. (2002) used 12 years of data from the Defense Meteorological Satellite Program (DMSP) for their analysis and showed that the yearly averaged solar flux index, F10.7, is well correlated (with a correlation coefficient of 0.98) with the EPD occurrence across all longitude sectors. Stolle et al. (2006) have also reported similar solar flux dependence of the EPD occurrence using 5 years of CHAllenging Minisatellite Payload (CHAMP) observations.

An interesting feature of the occurrence of EPDs is the seasonal/longitudinal (S/L) variability. Maruyama and Matuura (1984) found that at June (December) solstice, the EPDs show higher occurrence in the African and Pacific (South America and Atlantic) regions, while during equinoxes, the occurrence of EPDs shows less longitudinal dependence. Tsunoda (1985) suggested that the longitudinal gradient of the integrated *E* region conductivity is the main impact factor for controlling the EPD S/L dependence, with a higher occurrence during periods when the day-night terminator aligns with the magnetic field line. This explanation has been partially supported by similar S/L distributions of EPDs observed by different Low Earth Orbit (LEO) satellite missions, such as DMSP, Republic of China Satellite 1 (ROCSAT-1), CHAMP, Gravity and Recovery and Climate Experiment (GRACE), and Communication/Navigation Outage Forecasting System (C/NOFS; Burke, Gentile, et al., 2004; Burke, Huang, et al., 2004; Huang et al., 2014; Stolle et al., 2006; Su et al., 2006, 2008; Xiong et al., 2010).

Discussions above are mainly applied to the overall climatology of EPDs, while the postmidnight EPDs exhibit some different characteristics. Generally, the occurrence rate of postmidnight EPDs is lower than that during premidnight, but not negligible. Li et al. (2011) found that the postmidnight EPDs in the African and Pacific sectors during solar maximum summer are mostly the continuation of the EPDs generated at postsunset hours, different to the solar minimum summer EPDs in the Pacific, which are the continuation of EPDs generated around 2300 local time (LT) due to the *F* layer height increase. Nishioka et al. (2012) also found the uplift of the *F* layer to be highly connected to postmidnight EPDs and suggested that the recombination or trans-equatorial wind but not the eastward electric field leads to the uplift of the *F* layer. Differently, Yizengaw et al. (2013) suggested that the postmidnight EPDs are not the continuation of the postsunset EPDs and that eastward electric field does exist to initiate EPDs in postmidnight hours.

Another critical issue of EPDs is the effect on the trans-ionospheric radio waves, which is usually referred to as ionospheric scintillation. Extensive works from various aspects have been made to investigate the EPDs for forecasting the occurrence of radio wave scintillations (e.g., Aswathy & Manju, 2017; Carter et al., 2014; Deng et al., 2013). Paznukhov et al. (2012) reported that the occurrence of EPDs correlates well with GPS scintillations over Africa and that the depletion amplitude has an influence on the intensity of the scintillation. Recent work by Buchert et al. (2015) has revealed that GPS signal received by the Swarm satellites is sometimes interrupted, predominantly at the two plasma density crests of the equatorial ionization anomaly (EIA). Xiong, Stolle, et al. (2016) further presented a statistical study showing that the absolute density depletion of EPDs plays a key role in causing the GPS signal loss of Swarm satellites. When EPDs are found with absolute density depletion larger than 10×10^{11} m^{-3}, the chance causing GPS signal loss in at least one channel is as high as 95%; the chance of signal loss reduces to 30% when the depletion is lower than 10×10^{11} m^{-3}. These results confirm that the depletion amplitudes of EPDs are important for causing the interruption of the transionospheric radio signal, and therefore, it is worth to check their characteristics.

In this paper, we present a statistical study of the EPDs concerning their occurrence and amplitudes during both pre and postmidnight hours, using in situ plasma density measurements of Swarm satellites. Section 2 introduces the detection method and the definition of the amplitudes of EPDs. In section 3 statistics on magnetic LT (MLT) variations of EPDs, as well as IBI and Swarm signal loss events, followed by MLT distinguished S/L climatology of EPDs concerning both the occurrence and amplitudes are carried out. Discussions on the postmidnight EPDs and comparisons with previous studies are presented in the section 3.2. The manuscript ends with the conclusions.

2. Data Set and Processing

The magnetic latitude (MLAT) and MLT used in this study are based on the quasi-dipole coordinate system as described by Emmert et al. (2010).

2.1. Electron Density Measurements of Swarm

Swarm is the European Space Agency's (ESA) first constellation mission for Earth Observation (EO) at LEO, which consists of three identical satellites (Friis-Christensen et al., 2008), Alpha (A), Bravo (B), and Charlie (C). They were launched on 22 November 2013 in near-polar orbits at an initial altitude of about 500 km. Since 17 April 2014, the Swarm satellites were placed into two different polar orbits, Swarm A and C flying side-by-side (longitudinal separation of about 150 km) at an altitude of about 470 km, and the third one, Swarm B, at an altitude of about 520 km. Two Langmuir probes onboard of each Swarm satellite (set to high and low gain) provide the electron density along satellite track. In this study, we used the Level 1b data set of electron density, which is freely available by FTP to ESA-EO registered users in accordance with ESA EO Data Policy and is provided at a time resolution of 2 Hz.

2.2. Detection of EPDs and their Amplitudes

Different algorithms have been developed for identifying EPD events from satellite in situ measurements. Generally, the identification standard can be divided into two categories: The first one by using the relative density perturbation ($\Delta N/N$; e.g., Burke, Huang, et al., 2004; Huang et al., 2001, 2002; Kil & Heelis, 1998; Su et al., 2006), and the second one by using the absolute density perturbation (ΔN; e.g., Xiong et al., 2010). However, there is no generally accepted definition of EPD/equatorial plasma bubble based on its amplitude/depth. Kil and Heelis (1998) used the root mean square deviation with $\sigma = 1\%$ and $\sigma = 5\%$ for identifying EPDs from the observation of Atmosphere Explorer-E satellite. A smaller threshold of $\sigma = 0.3\%$ (from a logarithmic scale of plasma density) has been used by Su et al. (2006) for ROCSAT-1 measurements. With the same plasma density data, Burke, Gentile, et al. (2004) used density perturbation of $|\Delta \log N| > 0.015$ cm^{-3} for identifying EPDs. Huang et al. (2001, 2002) used the plasma density ratio for identifying EPDs from the DMSP observations. They have divided the EPD events into four groups according to their depletion depth. Considering that the background plasma density may differ at different altitudes. Xiong et al. (2010) set the thresholds of the absolute density perturbation to $5 \cdot 10^{10}$ m^{-3} and $3 \cdot 10^{10}$ m^{-3} for identifying the EPDs from CHAMP (at about 400 km) and GRACE (at about 500 km) observations, respectively. Huang et al. (2014) have compared the two identification standards by looking at the plasma density measurements of C/NOFS. They found that the occurrence probability of EPDs based on absolute density perturbation is higher in the evening sector and becomes much lower after midnight, while the occurrence probability based on relative density perturbation is lower in the evening sector but becomes higher after midnight in the June solstice. Additionally, they found that the occurrence pattern of the S4 index and its variation with MLT is in good agreement with the EPDs occurrence based on absolute density perturbation definition.

In this study, we take both the absolute and relative perturbations into account to identify the EPDs from Swarm electron density measurements. To illustrate our approach, two passes of Swarm A with EPDs detected are shown in Figure 1. The orbital arc between ±30° MLAT was first sorted out. Peak (purple triangles) and minimum (black asterisks) values are the primary features to find out. To exclude those depletions with negligible amplitudes and small spatial scale, two further limits have been set: (1) for the minimum values of neighboring depletion regions, if their latitudinal separation is less than 0.1° (about 12 km), they are then combined; (2) the absolute density depletion (the difference between the peak and minima) ΔNe should be larger than 5×10^{10} m^{-3}, and the relative depletion $\Delta Ne/Ne$ (Ne is the peak value) should be larger than 20%. Additionally, in order to distinguish the structure of EPDs from those large-scale ionospheric structures, such as EIA, the latitude separation between the peak and minimum values for each depletion should be less than 4° (about 440 km). By using this approach, we are mainly focused on plasma depletions with latitudinal scale sizes less than 440 km.

In the depletion regions, the background Ne (black curve) is linearly fitted between the peak values (using only the largest peak value of each 4° MLAT intersect with the peak value derived from the step introduced in the last paragraph), which is indeed the upper envelope of the measured Ne. For deriving the absolute depletion amplitude, we have subtracted the Swarm measurements (blue curve in Figure 1) in the depletion

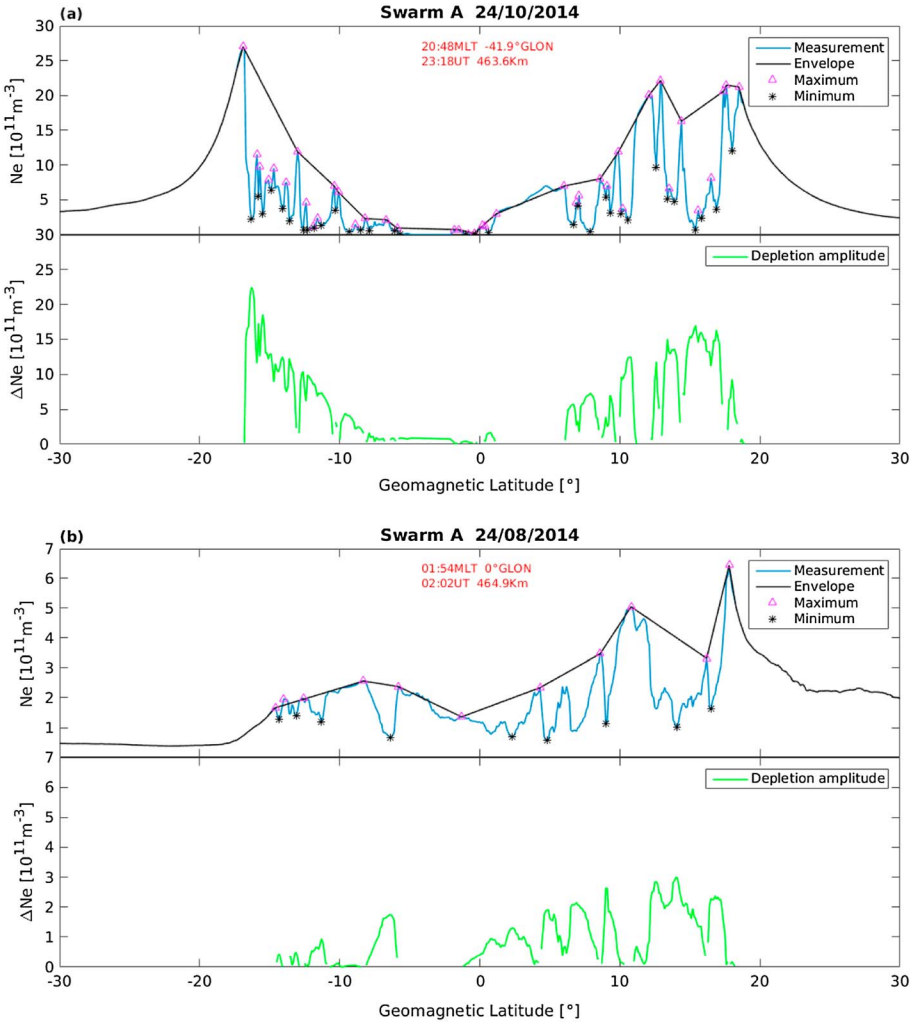

Figure 1. Two examples of equatorial plasma depletions (EPDs) observed by Swarm A on (a) 24 October 2014 during premidnight and (b) 24 August 2014 during postmidnight, respectively. In both top panels, the blue curves are the Swarm in situ electron density measurements, the pink triangles and black asterisks mark the maximum and minimum values of the depletion regions, and the black curves are the background profiles of the electron density. The green curves in both bottom panels are the depletion amplitudes of EPDs.

regions from the background *Ne*. The green curves at the bottom panel of Figure 1 represent the absolute depletion amplitudes of EPDs.

The data interval of the Swarm in situ electron density measurements used for the presented statistical analysis lasts from December 2013 to September 2017. In order to exclude the effect of geomagnetic disturbed time on our results, only the data set during geomagnetic quiet time ($Kp < 3$) is taken into account.

3. Results and Discussions

3.1. Magnetic Latitude and Magnetic Local Time Dependence of EPDs' Occurrence Rate and Amplitudes

The MLAT and MLT distributions of the EPD occurrence are binned into 2° of MLAT and 0.5 hr of MLT, and the occurrence rate is defined as the ratio between orbits with EPDs detected and the total orbits in each MLAT versus MLT bin (each bin consists about 1,100 Swarm orbits). From Figure 2a, we see that the EPDs are detected after 1900 MLT, and they are symmetrical about the magnetic equator within ±20° MLAT. The MLAT versus MLT distribution of EPDs is consistent with previous studies (e.g., Burke, Gentile, et al., 2004; Stolle et al., 2006; Su et al., 2006; Xiong et al., 2010), showing the largest occurrence rate around 2200 MLT

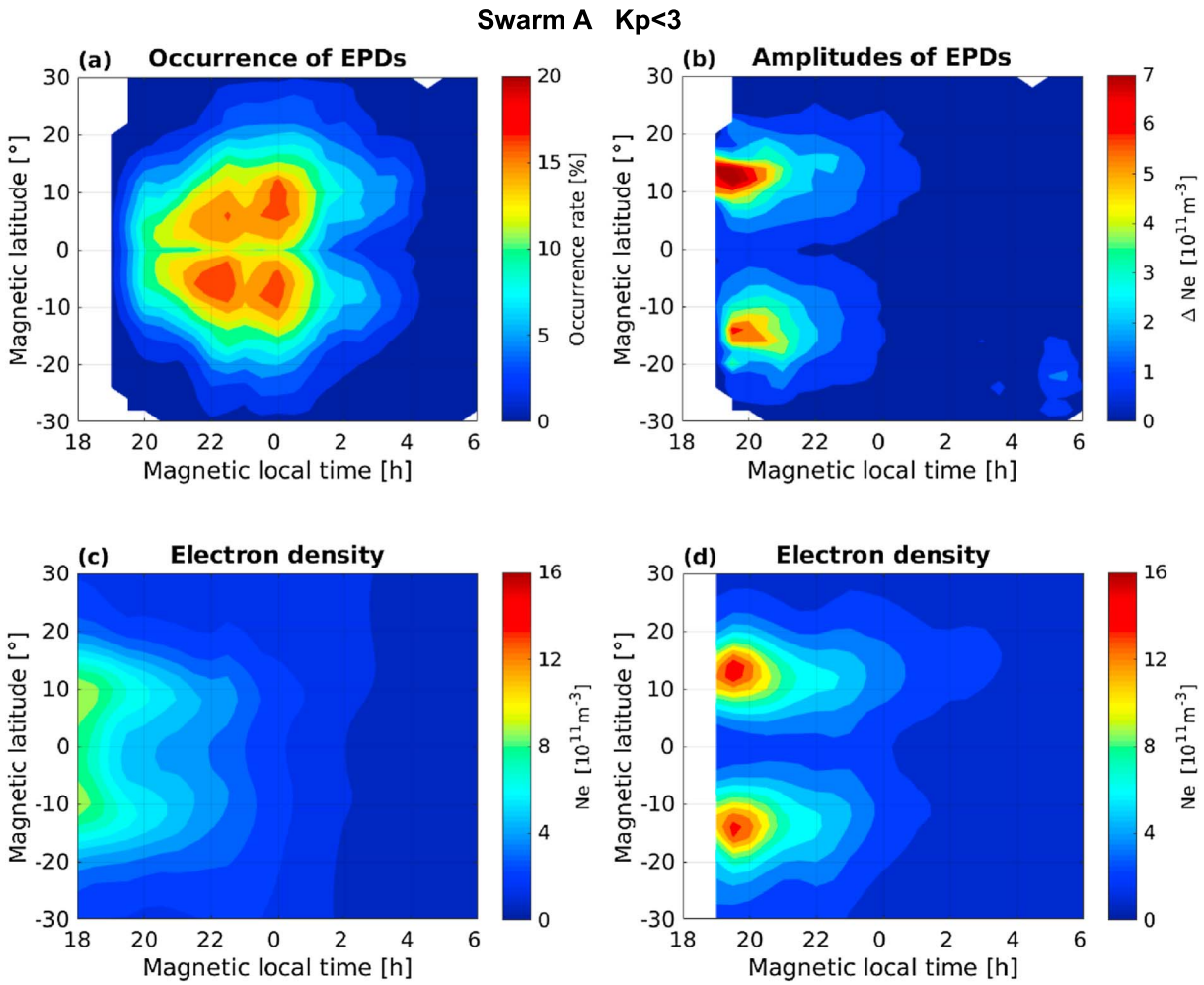

Figure 2. (a) MLAT and MLT distributions of the occurrence ratio of EPDs and (b) amplitudes of EPDs. (c) MLAT and MLT distributions of the background electron density from orbits without EPDs observed. (d) Similar to (c), but only from the orbits with EPDs detected.

until midnight. An interesting feature is that during earlier MLT, larger occurrence rate of EPDs is observed at latitudes closer to the magnetic equator than later MLT. This result strengthens the fact that EPDs are generated at the bottom side of the *F* region above the magnetic equator shortly after sunset, and later drift upward and extend to higher latitudes into both hemispheres.

Figure 2b presents the MLAT versus MLT distributions of EPDs as a function of the amplitude. Different to the occurrence rate, the amplitudes of EPDs show two peaks centered around ±15° MLAT shortly after sunset, and the two peaks are reduced quickly after 2200 MLT. Comparing to the peaks of the occurrence rate, the peaks of the depletion amplitudes appear at higher latitudes and at earlier MLT, which implies that the highest occurrence of EPDs does not always coincide with the largest depletion amplitude. The EPD amplitudes show similar MLT variations to those of the background plasma density at nightside to that as reported by (Xiong, Zhou, et al., 2016, their Figure 5). Around sunset at low latitudes, the enhanced eastward electric field in F region enlarges the equatorial fountain effect, causing the two crests of the EIA to get stronger and the trough above the dip equator to become deeper. Thus, we check the electron density derived with or without EPD-detected orbits. Figure 2c shows the MLAT versus MLT distribution of the electron density for the orbits without EPDs detected. As expected, the EIA presents the maximum values around 1830 MLT with their peaks centered around ±10° MLAT. Similarly, Figure 2d only considers orbits with EPDs detected. A significant enhancement exhibited regard to the intensity of the EIA when compared to Figure 2c. The largest values of the electron density appear around 1930 MLT centered about ±15° MLAT. The results show that

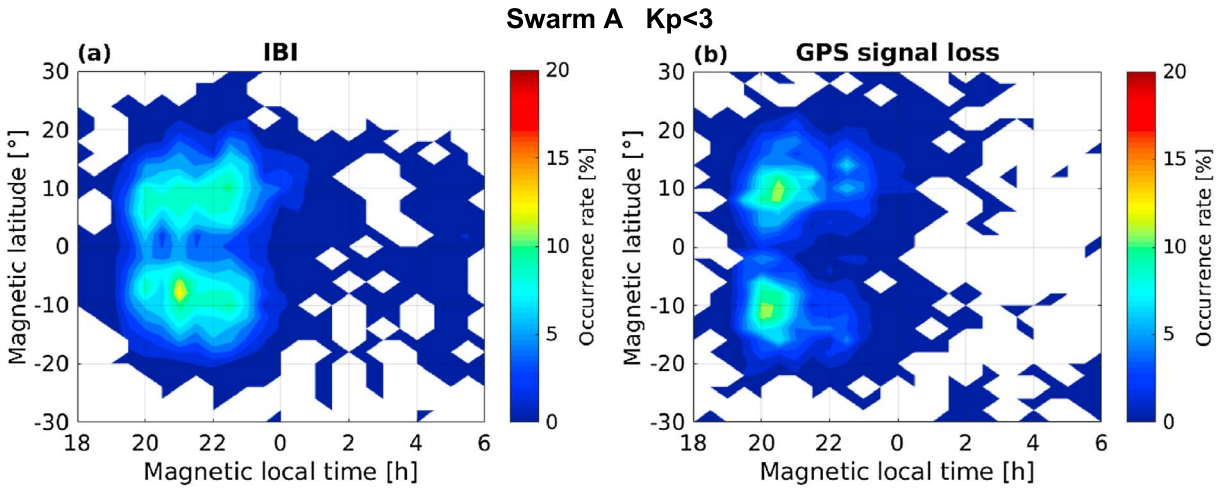

Figure 3. MLAT and MLT distributions of Swarm A derived (a) the occurrence ratio of IBI and (b) the Global Positioning System signal loss of the onboard receivers.

compared to those orbits without EPDs (Figure 2c), the orbits with EPDs detected correspond apparently to stronger upward $E \times B$ drift during PRE, thus more preference for EPDs formation, which is in agreement with previous results by Stolle et al. (2008) and Xiong et al. (2012).

For comparison, Figure 3a shows the MLAT versus MLT distribution of the occurrence of EPDs based on the IBI, which is a standard Level 2 product of the Swarm mission (Park et al., 2013). IBI provides information on EPD climatology itself as well as on the disturbance level of the magnetic field data by taking both electron density and magnetic field measurements into account. The distribution of EPD derived from the IBI shows (Figure 3a) similar results to the ones shown in Figure 2a, but with a lower occurrence rate. This is probably due to the fact that the amplitude of EPD must be larger enough to cause magnetic field fluctuations. Figure 3b presents the distribution of the loss of GPS signal (Xiong, Stolle, et al., 2016) as observed by Swarm A during a 3-year period from December 2013 to November 2016. The GPS signal losses are observed symmetrically about the magnetic equator between ±5° and ±20° MLAT and mainly between 1900 and 2300 MLT. The comparison between Figures 2 and 3 shows that the largest EPD amplitudes are located around 13° MLAT between 1900 and 2000 MLT in both hemispheres, while the maximal occurrence of GPS signal losses is centered at ±10° MLAT between 2000 and 2100 MLT. This disagreement can be interpreted as the low EPD occurrence rate of depletions with the largest amplitudes. Nevertheless, the losses of GPS signal share more features with the EPD amplitudes than with their occurrence rate.

3.2. Seasonal and Longitudinal Dependence of EPDs' Occurrence Rate

Figure 4 shows the global distribution of the occurrence rate of EPDs for three different seasons. The December solstice includes months from November to February, and equinoxes include March, April, September and October. June solstice includes months from May to August. The spatial resolution is 2° and 15° in response to MLAT and geographic longitude, and we plot the results in geographic coordinates. As already seen in Figure 2, both the occurrence rate and EPD amplitudes present lower values during post-midnight hours; therefore, the observations shown in Figure 4 are divided into two LT sectors, premidnight (1800–2400 MLT) and postmidnight (0000–0600 MLT). Again, only the observations during geomagnetic quiet time ($Kp < 3$) are taken into account. Finally, more than 100 orbits are obtained for each 15° longitude bin.

For the premidnight sector, the variation of EPD occurrence rate shows the largest preference at longitudes from American to Atlantic longitudes at December solstice, while wider longitude coverage (but with lower occurrence rate) appear at equinoxes. Comparing to the other two seasons, the occurrence of EPDs at June solstice months reduces substantially and shows peaks around Africa and Pacific longitudes. The S/L variability of the EPDs' occurrence shown here is consistent with previous reports of in situ measurements from other LEO satellites, for example, DMSP, ROCSAT-1, CHAMP, GRACE, and C/NOFS (Burke, Gentile, et al., 2004; Burke,

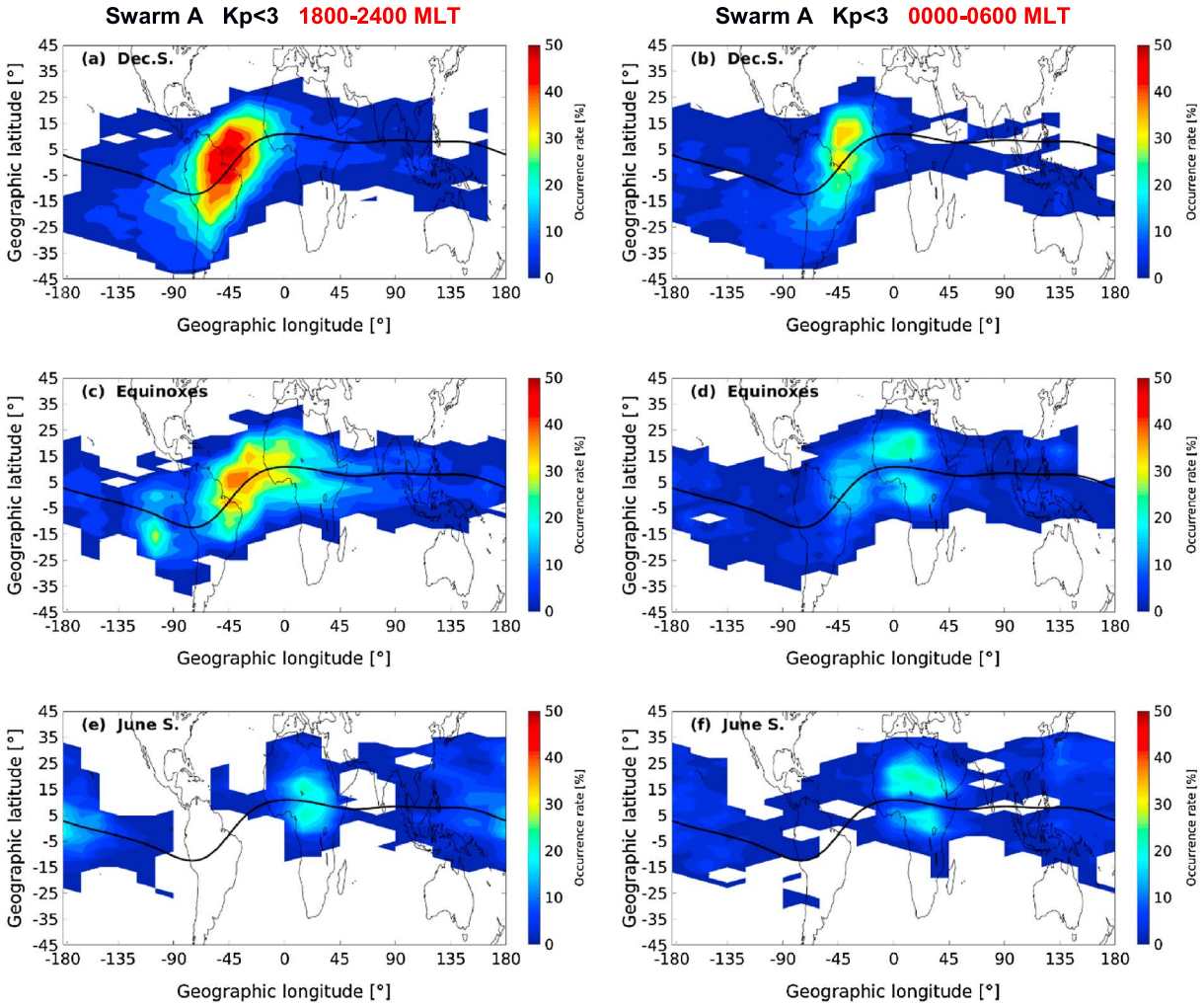

Figure 4. Geographic latitude and longitude distributions of the occurrence rate of equatorial plasma depletions for (left) premidnight 18:00–24:00 magnetic local time (MLT) and (right) postmidnight 00:00–06:00 MLT. The thick black curve in each figure represents the geomagnetic equator. Data have been divided into three seasons: (top) December solstice, (middle) equinoxes, and (bottom) June solstice.

Huang, et al., 2004; Huang et al., 2014; Stolle et al., 2006; Su et al., 2006, 2008; Xiong et al., 2010); therefore, we will not discuss this further.

An interesting feature of EPDs during postmidnight hours is that they always show the largest occurrence rate at African longitudes during equinoxes and June solstice (during December solstice they are shifted westward by about 45° to the Atlantic). Comparing to premidnight, the occurrence rate at American and Atlantic longitudes during December solstice and equinoxes is reduced at postmidnight. The situation changes at the African sector during both equinoxes and June solstice. Equinoxes present a relatively slighter reduction from premidnight to postmidnight (approximately from 35% to 15% over Atlantic and 30% to 28% over Africa) and a minor enhancement during June solstice at African longitudes.

The postmidnight EPDs are often associated with disturbed geomagnetic activity (Fejer et al., 1999); however, they have also been observed at quiet periods during the recent solar minimum (2008–2009; e.g., Dao et al., 2011; Huang et al., 2011; Yizengaw et al., 2013). Our results in Figure 4 reveal that the postmidnight EPDs are not only storm-related. During the recent solar minimum, 2008–2009 were regularly observed by the C/NOFS satellite according to Dao et al. (2011). In order to assess whether the postmidnight EPDs at the African sector are exclusively of solar minimum periods, we consider 9 years of CHAMP data which cover both high and low solar activity periods (2001–2009). The period covered by Swarm (from November 2013 to now) is quite low compared to the last solar maximum around 2002 and

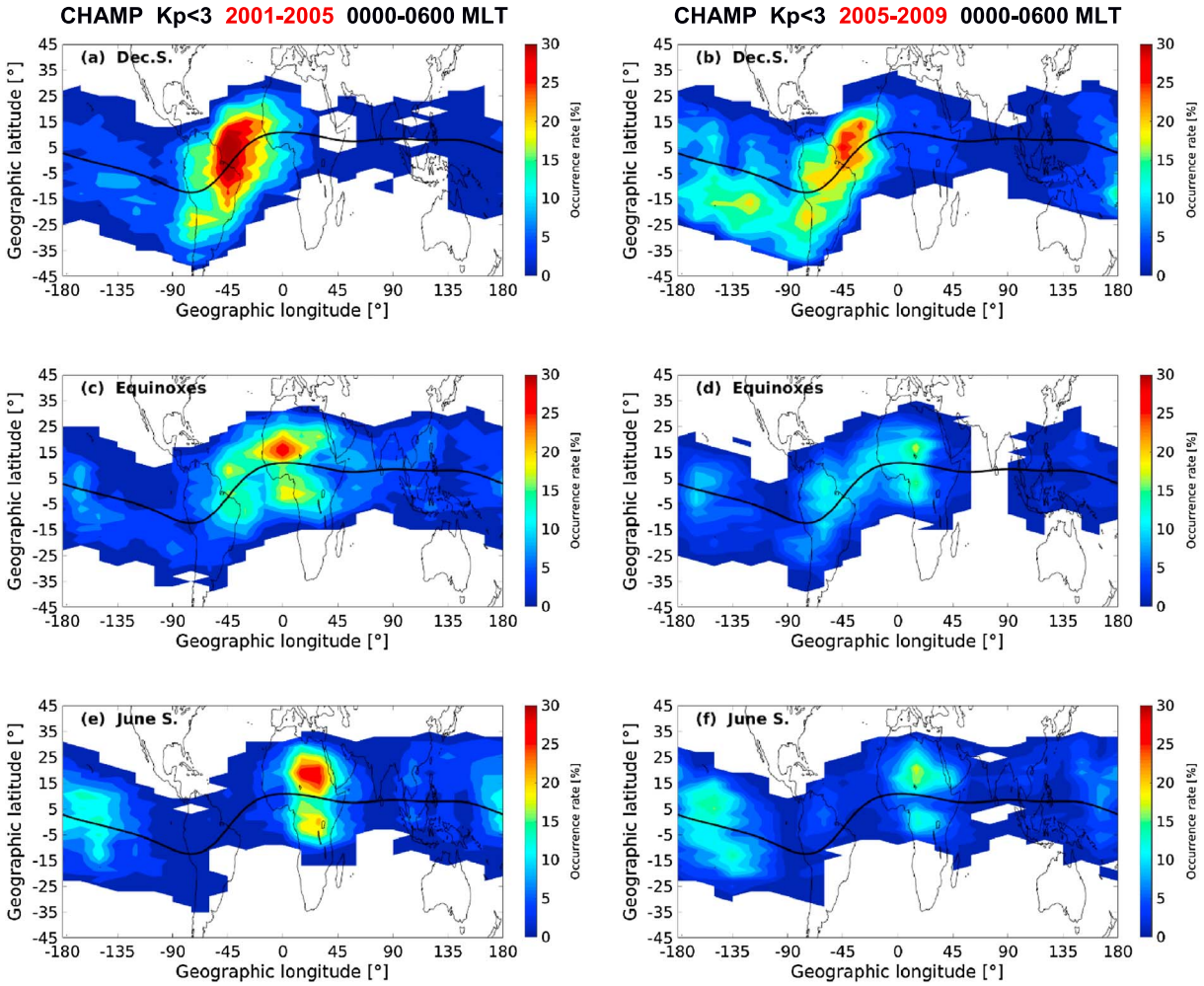

Figure 5. Postmidnight equatorial plasma depletion occurrence rate during two solar cycle phases in three seasons.

2003. In this study, the CHAMP observations are divided into two periods: 2001–2005 (high to moderate solar activity levels) and 2005–2009 (moderate to low solar activity levels). The same approach described in section 2 is applied to CHAMP in situ electron density measurements (time resolution of 15 s) with detection program adjusted regards to lower data cadence,

In Figure 5 the EPDs detected during quiet time postmidnight periods are depicted. Interestingly, the occurrence rate in December solstice over Pacific is larger during 2005–2009 than that in 2001–2005 (especially prominent at southeast Pacific), which is opposite in the other longitudes; during equinoxes and June solstice, the EPD occurrence in low solar activity years is also comparable to that in high solar activity years. On the other hand, the largest occurrence rate of postmidnight EPDs at African longitudes takes place during equinoxes and June solstice, regardless of the solar cycle. Then, based on the results obtained from both Swarm and CHAMP, it is understandable to say that postmidnight EPDs are a constant phenomenon at the African continent throughout the whole solar cycle.

As pointed out before, the generation of postmidnight EPDs is attributed to either fossil EPD generated during premidnight hours (Bhattacharyya et al., 2001; Li et al., 2011; MacDougall et al., 1998) or fresh EPD generated at postmidnight hours owing to local plasma instabilities (Retterer, 2009; Subbarao & Krishna Murthy, 1994; Yizengaw et al., 2013). Retterer (2009) pointed out that the postmidnight R-T instability induced by upward vertical drifts at that time can lift the ionospheric *F* layer to a higher altitude and leads to the plasma instability. However, based on both case and statistical studies, Yizengaw et al. (2013) explained that the postmidnight EPDs during June solstice are not a continuation of premidnight

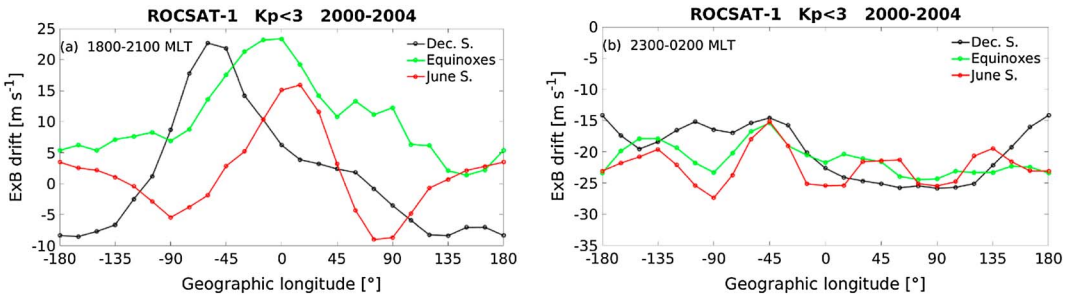

Figure 6. Vertical plasma drift measured by ROCSAT-1 during 2000–2004, (a) premidnight and (b) postmidnight. The black, green, and red curves represent December Solstice, equinoxes, and June solstice.

EPDs, initiated in the same way by the increase of the R-T instability growth rate due to the upward drift of the plasma. Although we cannot so far explain the generation mechanism of postmidnight EPDs, our results show that the occurrence rate of postmidnight EPDs at African longitudes during both equinoxes and June solstice is comparable (or even higher) when compared to that at premidnight hours. This phenomenon is more evident from CHAMP observations especially during solar maximum (not shown here). Based on ROCSAT-1 vertical plasma drift data, Fejer et al. (2008) found that the upward drift lasts longer till 2100 MLT over Africa during June solstice (their Figure 4) than any other longitude sectors and seasons. Similar finding had also been reported by Stolle et al. (2008) that at 0°E; the PRE peaks later and the upward drift decays slower during June solstice than December solstice and equinox, and there is a 2 to 3-hr time lag between PRE with the equatorial spread F occurrence, that is, topside irregularities take 2 to 3 hr to respond to the bottomside vertical plasma drift. When focused on African region, June solstice EPDs are detected throughout the whole night till 0400 MLT, but the occurrence peaks near midnight (not shown here). This gives a hint that the long-lasting upward drift could take the major responsibility for the postmidnight EPDs during June solstice, since the majority of which are detected right after 0000 MLT. On the one hand, the long-lasting upward drift that resulted in more occurrences of more EPDs after midnight does not mean no new EPDs are generated throughout postmidnight hours. On the other hand, long-lasting upward drift does not exist during equinoxes (Fejer et al., 2008), but the postmidnight EPDs still keep in a comparable amount compared to premidnight; if assuming there are some EPDs which cannot survive from premidnight to postmidnight, the existing of considerable amount of freshly generated EPDs is promised. We suggest that the postmidnight EPDs over Africa are the combined results from the continuing of former EPDs and newborn EPDs. Details about these newborn EPDs in postmidnight considering longitudinal/seasonal and solar cycle variations may need further investigation.

Figure 6 shows the averaged vertical plasma drift at the magnetic equator (within ±5° MLAT, approximation to $\mathbf{E} \times \mathbf{B}$ drift) measured by ROCSAT-1 satellite from 2000 to 2004. As introduced in last paragraph, it takes 2 to 3 hr for the topside irregularity response to vertical drift. From Figure 1a, the most frequent EPDs occur after 2000 MLT for the premidnight sector and before 0400 MLT for postmidnight. Thus, the data set has been divided into two MLT sectors 1800–2100 and 2300–0200 as premidnight and postmidnight related to the occurrence of EPDs. As expected, the peak values of the upward plasma drift, appearing at −60°E, −15°E , and 15°E for the three different seasons, correspond to the peak occurrence rate of the EPDs at premidnight hours as shown for Swarm A in Figure 4. The peak velocity is smaller in June solstice than the other two seasons, which meet the lower occurrence of EPDs. All these correlations support the previous results that the upward vertical drift is favorable for the generation of EPDs. But this explanation only applies to the situation at premidnight hours. Downward plasma drift during 2300–0200 MLT (Figure 6b) occurs worldwide during all the seasons. Moreover, the vertical drift at African longitudes is lower than the other longitudes during all three seasons, although most of the postmidnight EPDs are observed just above the African longitudes. Consider the seasonal effects over Africa, the vertical drifts of three seasons are in the same level but not for the occurrence of EPDs; lower occurrence rate is witnessed during December solstice. These disagreements imply that different to the premidnight sector, other factors rather than the vertical plasma drift may be more important for the generation of postmidnight EPDs. Further model simulations as well as ground-based observations are needed for addressing this point.

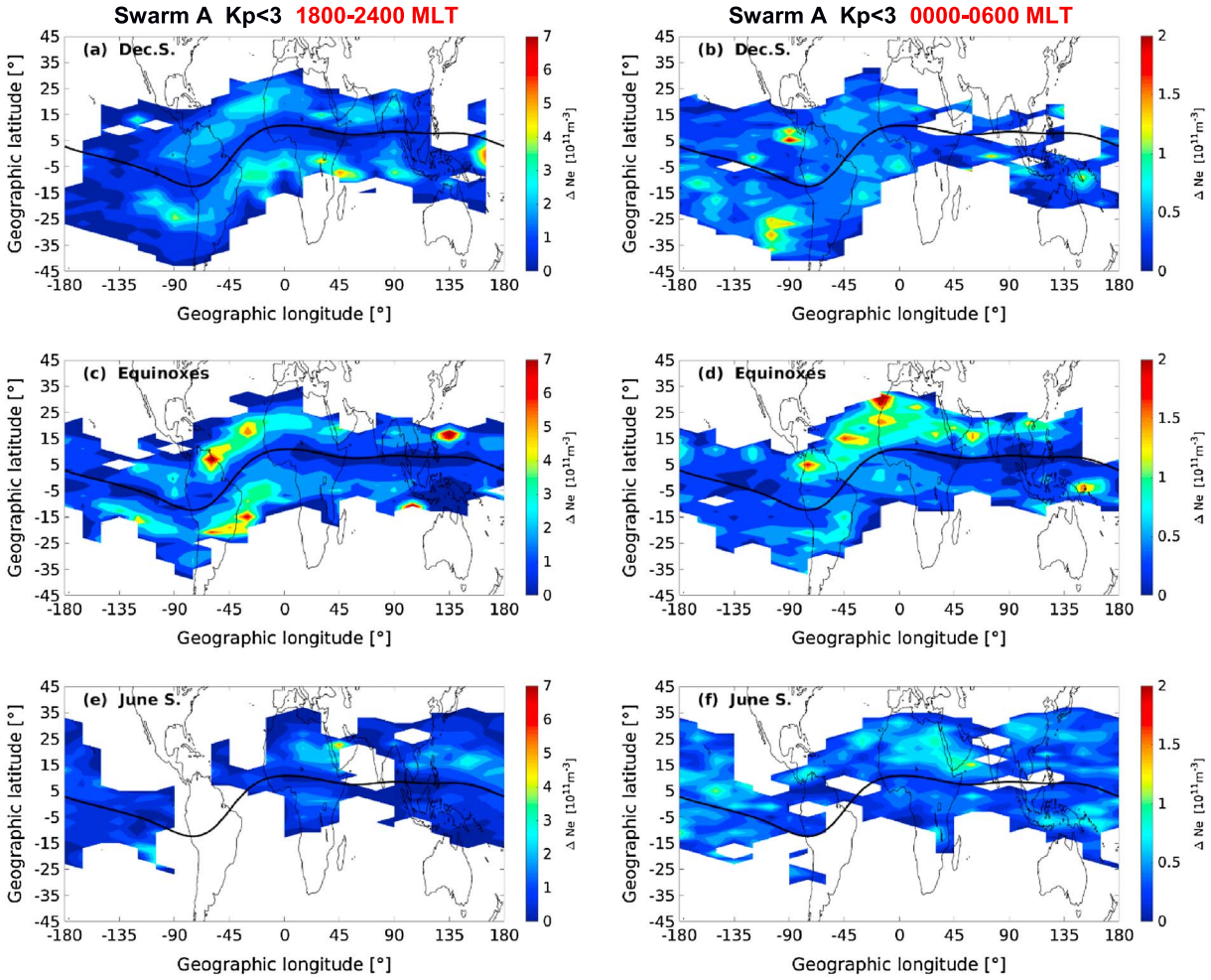

Figure 7. Similar to Figure 4, but for the amplitudes of equatorial plasma depletions.

3.3. Seasonal and Longitudinal Distributions of EPDs' Amplitudes

The global distribution of amplitudes of EPDs (Figure 7) is presented. Similarly, observations have been divided into (left) premidnight and (right) postmidnight hours, as well as into three different seasons. There are some isolated peaks located off equator, this discrete distribution is due to that there are few cases (less than 10) are detected, thus, those peaks cannot be used to represent the true climatology of amplitudes. However, to some extent, the signatures support the suggestion made in section 3.1 that amplitudes of EPDs are related to the background electron density. A general trend found here is that the depletion amplitudes are distributed more symmetrically around the magnetic equator for the premidnight hours (except June solstice) but not for the postmidnight sector. The amplitudes are basically larger in equinoxes compared to other months and in premidnight compared to premidnight. From a global view, the amplitudes of EPDs also show the longitudinal dependence for both MLT sectors; for example, largest amplitudes are found in America-to-Africa sector of the northern hemisphere during equinox months (Figure 7d). In general, when making a comparison with the occurrence of EPDs (Figure 4), the amplitudes exhibit a totally different longitudinal pattern.

As suggested in section 3.1, the depletion amplitude dependence on the MLT shares the similar pattern with background electron density rather than the occurrence. We further checked the background electron density in comparison from the longitudinal perspective, and the result is presented in Figure 8. Please note that only orbits detected with EPDs have been taken into account. For the premidnight sector, typical features of EIA of three seasons can be identified, and a good agreement is found when looking back to amplitudes maps. Moreover, for the postmidnight sector as the EIA signal is vanished, while the electron

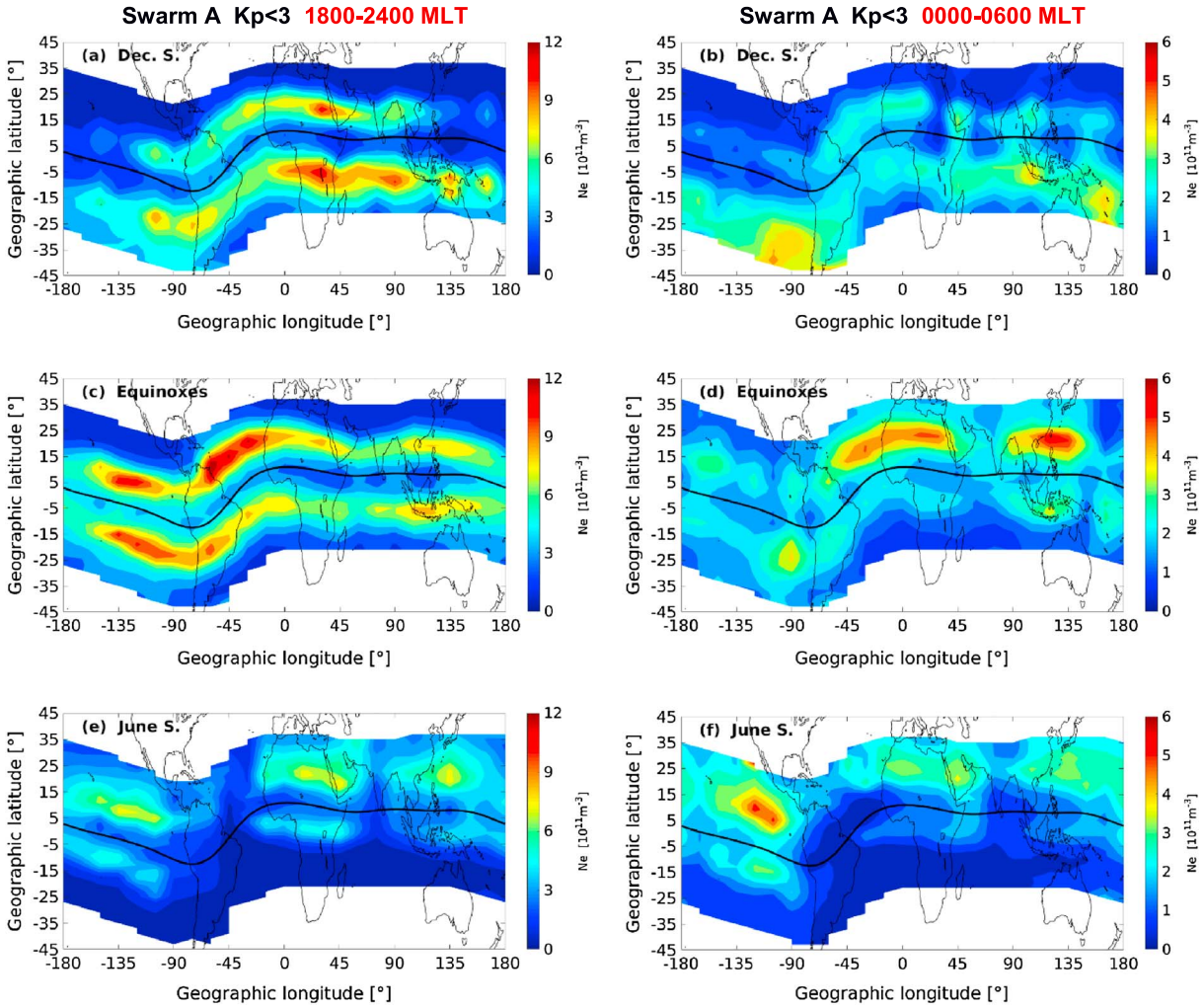

Figure 8. Similar to Figure 4, but for the background electron density, only orbits with equatorial plasma depletion detected counts.

density has decreased, the hemispheric asymmetry and longitudinal wave structure are strengthened especially for equinoxes (Figure 8d). This electron density distribution explains the longitudinal variation of the amplitudes of postmidnight EPDs regarding different seasons; evidence is witnessed as almost every region of maximum amplitudes correspondingly encountered a peak density. Thus, we conclude that the amplitudes of EPDs are largely depending on background electron density globally, as expected.

4. Summary

In this study, we have used the in situ electron density measurements from Swarm satellites to investigate the climatology of EPDs concerning their occurrence and amplitudes. The main findings are summarized as follows:

1. The EPDs show largest occurrence rate between 2100 and 0000 MLT and in the vicinity of the equator, while the EPDs with largest depletion amplitudes appear earlier between 1900 and 2100 MLT located several degrees off the equator. From both MLT and longitudinal perspectives, the depletion amplitudes are much more closely related to the intensity of background electron density rather than the occurrence rate of EPDs.
2. For the first time, we compared our results with both GPS signal loss events and Swarm Level-2 product, IBI. The occurrence rate of EPDs derived from the orbital profiles of electron density shows similar MLAT and MLT distribution with that derived from the IBI, and our results confirm that the Swarm GPS signal loss

of receiver is more affected by the EPDs with larger depletion amplitudes appearing at earlier MLT (1900–2100 MLT).

3. The observations from CHAMP mission show that the postmidnight EPDs at African longitudes during equinoxes and June solstice appear not only during solar minimum years but also at the solar maximum condition.
4. From a global view, the occurrence rate of postmidnight EPDs is generally reduced compared to the premidnight; however, African sectors is an exception for equinoxes and June solstice. Equinoxes perform a slighter reduction from premidnight to postmidnight over Africa, and June solstice even experienced an increase.
5. We conclude that postmidnight occurrence consists both the continuation of premidnight EPDs as well as the freshly generated EPDs, and the weight allocation of each source depends on the season, longitude, and solar cycle, which requires further checking. Different from the premidnight EPDs, the postmidnight initiated EPDs seem to be less related to the *F* region vertical plasma drift.

Acknowledgments
The European Space Agency is acknowledged for providing the Swarm data. The official Swarm website is http://earth.esa.int/swarm, and the server for Swarm data distribution is ftp://swarm-diss.eo.esa.int. The CHAMP mission was sponsored by the Space Agency of the German Aerospace Center (DLR) through funds of the Federal Ministry of Economics and Technology. The CHAMP in situ electron density data (CH-ME-2-PLP) is available at the Information System and Data Center (ISDC) of the German Research Centre for Geosciences (GFZ). The vertical drift data from ROCSAT-1 were provided by the National Central University of Taiwan, which can be downloaded from http://sdbweb.ss.ncu.edu.tw/ipei_download.html. The work of Xin Wan is supported by National Nature Science Foundation of China (41674153, 41521063, and 41431076).

References

Aswathy, R. P., & Manju, G. (2017). Gravity wave control on ESF day-to-day variability: An empirical approach. *Journal of Geophysical Research: Space Physics*, *122*, 6791–6798. https://doi.org/10.1002/2017JA023983

Basu, S., Groves, K. M., Basu, S., & Sultan, P. J. (2002). Specification and forecasting of scintillations in communication/navigation links: Current status and future plans. *Journal of Atmospheric and Solar - Terrestrial Physics*, *64*(16), 1745–1754. https://doi.org/10.1016/S1364-6826(02)00124-4

Basu, S., MacKenzie, E., & Basu, S. (1988). Ionospheric constraints on VHF/UHF communications links during solar maximum and minimum periods. *Radio Science*, *23*, 363–378. https://doi.org/10.1029/RS023i003p00363

Bhattacharyya, A., Basu, S., Groves, K. M., Valladares, C. E., & Sheehan, R. (2001). Dynamics of equatorial *F* region irregularities from spaced receiver scintillation observations. *Geophysical Research Letters*, *28*, 119–122. https://doi.org/10.1029/2000GL012288

Booker, H. G., & Wells, H. W. (1938). Scattering of radio waves by the *F*-region of the ionosphere. *Journal of Geophysical Research*, *43*, 249–256. https://doi.org/10.1029/TE043i003p00249

Buchert, S., Zangerl, F., Sust, M., André, M., Eriksson, A., Wahlund, J., & Opgenoorth, H. (2015). SWARM observations of equatorial electron densities and topside GPS track losses. *Geophysical Research Letters*, *42*, 2088–2092. https://doi.org/10.1002/2015GL063121

Burke, W. J., Gentile, L. C., Huang, C. Y., Valladares, C. E., & Su, S. Y. (2004). Longitudinal variability of equatorial plasma bubbles observed by DMSP and ROCSAT-1. *Journal of Geophysical Research*, *109*, A12301. https://doi.org/10.1029/2004JA010583

Burke, W. J., Huang, C. Y., Gentile, L. C., & Bauer, L. (2004). Seasonal-longitudinal variability of equatorial plasma bubble occurrence. *Annales Geophysicae*, *22*(9), 3089–3098. https://doi.org/10.5194/angeo-22-3089-2004

Carter, B. A., Retterer, J. M., Yizengaw, E., Wiens, K., Wing, S., Groves, K., et al. (2014). Using solar wind data to predict daily GPS scintillation occurrence in the African and Asian low-latitude regions. *Geophysical Research Letters*, *41*, 8176–8184. https://doi.org/10.1002/2014GL062203

Carter, B. A., Zhang, K., Norman, R., Kumar, V. V., & Kumar, S. (2013). On the occurrence of equatorial *F*-region irregularities during solar minimum using radio occultation measurements. *Journal of Geophysical Research: Space Physics*, *118*, 892–904. https://doi.org/10.1002/jgra.50089

Dabas, R. S., Singh, L., Lakshmi, D. R., Subramanyam, P., Chopra, P., & Garg, S. C. (2003). Evolution and dynamics of equatorial plasma bubbles: Relationships to E × B drift, postsunset total electron content enhancements and equatorial electrojet strength. *Radio Science*, *38*(4), 1075. https://doi.org/10.1029/2001RS002586

Dao, E., Kelley, M. C., Roddy, P., Retterer, J., Ballenthin, J. O., de La Beaujardiere, O., & Su, Y.-J. (2011). Longitudinal and seasonal dependence of nighttime equatorial plasma density irregularities during solar minimum detected on the C/NOFS satellite. *Geophysical Research Letters*, *38*, L10104. https://doi.org/10.1029/2011GL047046

Deng, B., Huang, J., Liu, W., Xu, J., & Huang, L. (2013). GPS scintillation and TEC depletion near the northern crest of equatorial anomaly over South China. *Advances in Space Research*, *51*(3), 356–365. https://doi.org/10.1016/j.asr.2012.09.008

Emmert, J. T., Richmond, A. D., & Drob, D. F. (2010). A computationally compact representation of magnetic-apex and quasi-dipole coordinates with smooth base vectors. *Journal of Geophysical Research*, *115*, A08322. https://doi.org/10.1029/2010JA015326

Fejer, B. G., dePaula, E. R., Heelis, R. A., & Hanson, W. B. (1995). Global equatorial ionospheric vertical plasma drifts measured by the AE-E satellite. *Journal of Geophysical Research*, *100*, 5769–5776. https://doi.org/10.1029/94JA03240

Fejer, B. G., Jensen, J. W., & Su, S.-Y. (2008). Quiet time equatorial *F* region vertical plasma drift model derived from ROCSAT-1 observations. *Journal of Geophysical Research*, *113*, A05304. https://doi.org/10.1029/2007JA012801

Fejer, B. G., Scherliess, L., & de Paula, E. R. (1999). Effects of the vertical plasma drift velocity on the generation and evolution of equatorial spread *F*. *Journal of Geophysical Research*, *104*, 19,859–19,870. https://doi.org/10.1029/1999JA900271

Friis-Christensen, E., Lühr, H., Knudsen, D., & Haagmans, R. (2008). Swarm—An Earth observation mission investigating Geospace. *Advances in Space Research*, *41*(1), 210–216. https://doi.org/10.1016/j.asr.2006.10.008

Huang, C.-S., de La Beaujardiere, O., Roddy, P. A., Hunton, D. E., Liu, J. Y., & Chen, S. P. (2014). Occurrence probability and amplitude of equatorial ionospheric irregularities associated with plasma bubbles during low and moderate solar activities (2008–2012). *Journal of Geophysical Research: Space Physics*, *119*, 1186–1199. https://doi.org/10.1002/2013JA019212

Huang, C.-S., de La Beaujardiere, O., Roddy, P. A., Hunton, D. E., Pfaff, R. F., Valladares, C. E., & Ballenthin, J. O. (2011). Evolution of equatorial ionospheric plasma bubbles and formation of broad plasma depletions measured by the C/NOFS satellite during deep solar minimum. *Journal of Geophysical Research*, *116*, A03309. https://doi.org/10.1029/2010JA015982

Huang, C. Y., Burke, W. J., Machuzak, J. S., Gentile, L. C., & Sultan, P. J. (2001). DMSP observations of equatorial plasma bubbles in the topside ionosphere near solar maximum. *Journal of Geophysical Research*, *106*, 8131–8142. https://doi.org/10.1029/2000JA000319

Huang, C. Y., Burke, W. J., Machuzak, J. S., Gentile, L. C., & Sultan, P. J. (2002). Equatorial plasma bubbles observed by DMSP satellites during a full solar cycle: Toward a global climatology. *Journal of Geophysical Research*, *107*(A12), 1434. https://doi.org/10.1029/2002JA009452

Hudson, M. K., & Kennel, C. F. (1975). Linear theory of equatorial spread F. *Journal of Geophysical Research*, *80*, 4581–4590. https://doi.org/10.1029/JA080i034p04581

Kelley, M. C., LaBelle, J., Kudeki, E., Fejer, B. G., Basu, S. A., Basu, S., et al. (1986). The condor equatorial spread F campaign: Overview and results of the large-scale measurements. *Journal of Geophysical Research*, *91*, 5487–5503. https://doi.org/10.1029/JA091iA05p05487

Kelley, M. C., Larsen, M. F., LaHoz, C., & McClure, J. P. (1981). Gravity wave initiation of equatorial spread F: A case study. *Journal of Geophysical Research*, *86*, 9087–9100. https://doi.org/10.1029/JA086iA11p09087

Kil, H., & Heelis, R. A. (1998). Global distribution of density irregularities in the equatorial ionosphere. *Journal of Geophysical Research*, *103*, 407–417. https://doi.org/10.1029/97JA02698

Li, G., Ning, B., Abdu, M. A., Yue, X., Liu, L., Wan, W., & Hu, L. (2011). On the occurrence of postmidnight equatorial F region irregularities during the June solstice. *Journal of Geophysical Research*, *116*, A04318. https://doi.org/10.1029/2010JA016056

MacDougall, J. W., Abdu, M. A., Jayachandran, P. T., Cecile, J.-F., & Batista, I. S. (1998). Presunrise spread F at Fortaleza. *Journal of Geophysical Research*, *103*, 23,415–23,425. https://doi.org/10.1029/98JA01949

Maruyama, T., & Matuura, N. (1984). Longitudinal variability of annual changes in activity of equatorial spread F and plasma bubbles. *Journal of Geophysical Research*, *89*, 10,903–10,912. https://doi.org/10.1029/JA089iA12p10903

Nishioka, M., Otsuka, Y., Shiokawa, K., Tsugawa, T., Effendy, P., Supnithi, T. N., & Murata, K. T. (2012). On post-midnight field-aligned irregularities observed with a 30.8-MHz radar at a low latitude: Comparison with F-layer altitude near the geomagnetic equator. *Journal of Geophysical Research*, *117*, A08337. https://doi.org/10.1029/2012JA017692

Ott, E. (1978). Theory of Rayleigh-Taylor bubbles in the equatorial ionosphere. *Journal of Geophysical Research*, *83*, 2066–2070. https://doi.org/10.1029/JA083iA05p02066

Park, J., Noja, M., Stolle, C., & Lühr, H. (2013). The Ionospheric Bubble Index deduced from the magnetic field and plasma observations onboard Swarm. *Earth, Planets and Space*, *65*(11), 1333–1344. https://doi.org/10.5047/eps.2013.08.005

Paznukhov, V. V., Carrano, C. S., Doherty, P. H., Groves, K. M., Caton, R. G., Valladares, C. E., et al. (2012). Equatorial plasma bubbles and L-band scintillations in Africa during solar minimum. *Annales Geophysicae*, *30*(4), 675–682. https://doi.org/10.5194/angeo-30-675-2012

Retterer, J. M. (2009). Late-night irregularities at solar min or the curious incident of the dog in the night, CEDAR Workshop, Santa Fe, New Mexico, 28 June - 2 July.

Singh, S., Johnson, F. S., & Power, R. A. (1997). Gravity wave seeding of equatorial plasma bubbles. *Journal of Geophysical Research*, *102*, 7399–7410. https://doi.org/10.1029/96JA03998

Stolle, C., Lühr, H., & Fejer, B. G. (2008). Relation between the occurrence rate of ESF and the equatorial vertical plasma drift velocity at sunset derived from global observations. *Annales Geophysicae*, *26*(12), 3979–3988. https://doi.org/10.5194/angeo-26-3979-2008

Stolle, C., Lühr, H., Rother, M., & Balasis, G. (2006). Magnetic signatures of equatorial spread F as observed by the CHAMP satellite. *Journal of Geophysical Research*, *111*, A02304. https://doi.org/10.1029/2005JA011184

Su, S.-Y., Chao, C. K., & Liu, C. H. (2008). On monthly/seasonal/longitudinal variations of equatorial irregularity occurrences and their relationship with the postsunset vertical drift velocities. *Journal of Geophysical Research*, *113*, A05307. https://doi.org/10.1029/2007JA012809

Su, S.-Y., Liu, C. H., Ho, H. H., & Chao, C. K. (2006). Distribution characteristics of topside ionospheric density irregularities: Equatorial versus midlatitude regions. *Journal of Geophysical Research*, *111*, A06305. https://doi.org/10.1029/2005JA011330

Subbarao, K. S. V., & Krishna Murthy, B. V. (1994). Seasonal variations of equatorial spread-F. *Annales Geophysicae*, *12*(1), 33–39. https://doi.org/10.1007/s00585-994-0033-4

Sultan, P. J. (1996). Linear theory and modeling of the Rayleigh-Taylor instability leading to the occurrence of equatorial spread F. *Journal of Geophysical Research*, *101*, 26,875–26,891. https://doi.org/10.1029/96JA00682

Tsunoda, R. T. (1985). Control of the seasonal and longitudinal occurrence of equatorial scintillations by the longitudinal gradient in integrated E region Pedersen conductivity. *Journal of Geophysical Research*, *90*, 447–456. https://doi.org/10.1029/JA090iA01p00447

Xiong, C., Lühr, H., Ma, S. Y., Stolle, C., & Fejer, B. G. (2012). Features of highly structured equatorial plasma irregularities deduced from CHAMP observations. *Annales Geophysicae*, *30*(8), 1259–1269. https://doi.org/10.5194/angeo-30-1259-2012

Xiong, C., Park, J., Lühr, H., Stolle, C., & Ma, S. Y. (2010). Comparing plasma bubble occurrence rates at CHAMP and GRACE altitudes during high and low solar activity. *Annales Geophysicae*, *28*(9), 1647–1658. https://doi.org/10.5194/angeo-28-1647-2010

Xiong, C., Stolle, C., & Lühr, H. (2016). The Swarm satellite loss of GPS signal and its relation to ionospheric plasma irregularities. *Space Weather*, *14*, 563–577. https://doi.org/10.1002/2016SW001439

Xiong, C., Zhou, Y.-L., Lühr, H., & Ma, S.-Y. (2016). Diurnal evolution of the F region electron density local time gradient at low and middle latitudes resolved by the Swarm constellation. *Journal of Geophysical Research: Space Physics*, *121*, 9075–9089. https://doi.org/10.1002/2016JA023034

Yizengaw, E., Retterer, J., Pacheco, E. E., Roddy, P., Groves, K., Caton, R., & Baki, P. (2013). Postmidnight bubbles and scintillations in the quiet-time June solstice. *Geophysical Research Letters*, *40*, 5592–5597. https://doi.org/10.1002/2013GL058307